

# TempEE: Temporal-Spatial Parallel Transformer for Radar Echo Extrapolation Beyond Auto-Regression

Shengchao Chen, Ting Shu, Huan Zhao, Guo Zhong and Xunlai Chen

**Abstract**—The meteorological radar reflectivity data, also known as echo, plays a crucial role in predicting precipitation and enabling accurate and fast forecasting of short-term heavy rainfall without the need for complex Numerical Weather Prediction (NWP) model. Compared to conventional model, Deep Learning (DL)-based radar echo extrapolation algorithms are more effective and efficient. However, the development of highly reliable and generalized algorithms is hindered by three main bottlenecks: cumulative error spreading, imprecise representation of sparse echo distribution, and inaccurate description of non-stationary motion process. To address these issues, this paper presents a novel radar echo extrapolation algorithm that utilizes temporal-spatial correlation features and the Transformer technology. The algorithm extracts features from multi-frame echo images that accurately represent non-stationary motion processes for precipitation prediction. The proposed algorithm uses a novel parallel encoder based on Transformer technology to effectively and automatically extract echoes’ temporal-spatial features. Furthermore, a Multi-level Temporal-Spatial attention mechanism is adopted to enhance the ability to perceive global-local information and highlight the task-related feature regions in a lightweight way. The proposed method’s effectiveness has been validated on the classic radar echo extrapolation task using the real-world dataset. Numerous experiments have further demonstrated the effectiveness and necessity of various components of the proposed method.

**Index Terms**—Radar echo extrapolation, Precipitation now-casting, Deep Learning, Transformer, Self-attention.

This work was supported in part by the National Key Research and Development Program of China for Intergovernmental Cooperation under Grant 2019YFE0110100, in part by the National Natural Science Foundation of China under Grant 42105145, in part by the Guangdong Province Natural Science Foundation under Grant 2023A1515011438, in part by the Science and technology innovation team project of Guangdong Meteorological Bureau under Grant GRMCTD202104, in part by the Innovation and Development Project of China Meteorological Administration under Grant CXFZ2022J002 and in part by the Shenzhen Hong Kong Macao science and technology plan project under Grant SGDX20210823103537035. (Corresponding authors: Ting Shu, Guo Zhong)

Shengchao Chen is with Guangdong-Hongkong-Macao Greater Bay Area Weather Research Center for Monitoring Warning and Forecasting (Shenzhen Institute of Meteorological Innovation), Shenzhen 518125, China, also with Australian Artificial Intelligence Institute, School of Computer Science, FEIT, University of Technology Sydney, Sydney, Ultimo 2007, NSW, Australia (email: pavelchen@ieee.org)

Ting Shu is with Guangdong-Hongkong-Macao Greater Bay Area Weather Research Center for Monitoring Warning and Forecasting (Shenzhen Institute of Meteorological Innovation), Shenzhen 518125, China (email: shutting@gbamwf.com)

Huan Zhao is with School of Electrical and Electronic Engineering, Nanyang Technological University, Singapore (email: huan.zhao@ntu.edu.sg)

Guo Zhong is with School of Information Science and Technology, Guangdong University of Foreign Studies, Guangzhou 510006, China (email: zhg102003@163.com)

Xunlai Chen is with Shenzhen Meteorological Bureau / Shenzhen Key laboratory of severe weather in south China, Shenzhen 518125, China (email: cxlxun@163.com)

## I. INTRODUCTION

**E**XTRME meteorological events, such as typhoons and thunderstorms, can cause heavy rainfall within local areas in a short period. These events can lead to life-threatening accidents, such as flash floods, mud-rock flows, urban waterlogging, and landslides, and can cause significant damage to infrastructure [1]. Hence, accurate, reliable, and timely precipitation forecasting is essential to mitigate the effects of extreme weather. While Numerical Weather Prediction (NWP) models [2], [3] can account for a wide range of atmospheric physical constraints and explain some long-term weather processes, their uncertainties, high computational cost, and significant storage resource limit their effectiveness for short-term precipitation forecasting. Therefore, alternative methods that provide more stable, real-time, and cost-effective short-term precipitation forecasts should be explored [4].

The predicting of future continuous information about precipitation cloud movement through meteorological radar echos extrapolation is crucial for short-term precipitation forecasting. However, traditional radar echo extrapolation methods [5]–[9], such as using motion vectors to model changes in echo patterns [5], have limited accuracy in modeling nonlinear variations and uncertainties in complex weather systems. Artificial Intelligence (AI), particularly Deep Learning (DL), have provided alternative methods [10]–[19] for radar echo extrapolation. These methods employ temporal-spatial sequence forecasting, where the model learns temporal-spatial information from historical observations to predict future echo motion.

DL-based strategies for radar extrapolation can be categorized into two types: those based on Convolutional Neural Networks (CNN) [11], [20]–[23] and those based on Recurrent Neural Networks (RNN) [12], [16]–[19], [24]–[27]. The former is better at modeling spatial representation of radar echos, while RNN-based is superior in capturing temporal correlations among various motion processes of radar echos. To overcome the limitations of these models, recent studies have proposed hybrid models [11], [12], [19] that combine CNN and RNN. However, these models are not without limitations, such as being vulnerable to weak sparse echo features and non-stationary weather processes. Additionally, as extrapolation time increases, these models may suffer from a rapid decay of echo refinement and prediction accuracy, which could potentially impact their reliability and availability.

To address these limitations, this paper proposes a novel deep-learning model called the **Temporal-Spatial Parallel Transformer for Radar Echo Extrapolation** (dubbed *TempEE*). The *TempEE* constructs a comprehensive representation of

the complex temporal-spatial relationships between historical observations and future echoes for accurate and timely precipitation forecasting. Compared to the auto-regression-based extrapolation method, *TempEE* uses a one-step forward strategy to learn the distribution of radar echoes and motion trends in parallel, resulting in an advanced temporal and spatial representation. Furthermore, a new attentional fraction calculation strategy is proposed in the overall framework to represent the global-local echo distribution with low computational effort. *TempEE* is an innovative approach to improving the accuracy of precipitation forecasting based on radar echo image extrapolation tasks.

The main contributions of this work are summarized in four-fold:

- A Transformer-based model is proposed for precipitation forecasting, which reliably predicts complex radar echo distributions and motion trends, including dense and sparse distributions as well as stationary and non-stationary motion trends. The model outperforms auto-regression-based extrapolation algorithms in terms of effectiveness.
- To flexibly and effectively capture non-stationary motion trends and sparse radar echo distributions, we propose a parallel encoder structure comprising a Temporal Encoder (TE) and a Spatial Encoder (SE). The TE creates temporal correlations between echo distributions, while the SE deals with the spatial representation of echo distributions.
- We introduce a Temporal-Spatial Decoder (TSD) based on reverse random sampling to enhance the ability to extract global-local information and spatiotemporal correlations. During the training phase, this approach randomly provides prior knowledge, which prompts the model to learn a complete representation of the trend. Additionally, we adopt a Multi-level Spatio-Temporal Attention (MSTA) to refine echo features in a lightweight manner with low computational complexity.
- We train and test the proposed model on a real-world radar echo image dataset and perform an extensive study to analyze the contribution of each component. The experimental results demonstrate that the model accurately predicts both stationary and non-stationary weather processes and significantly outperforms other DL-based models in terms of prediction accuracy and efficiency.

The remainder of this work is in the following: Section II reviews related works. Section III describes the proposed model in detail. The the specific implementation details of the experiment and the results are given in Section IV. The last section (Section V) concludes this work.

## II. RELATED WORKS

This section summarizes the relevant representative approaches on this work, including traditional radar echo extrapolation methods, DL-based radar echo extrapolation, and vision Transformers (ViTs).

### A. Traditional Radar Echo Extrapolation Methods

The conventional numerical echo extrapolation models require determining the motion region. The Tracking Radar

Echoes Correlation (TREC) algorithm [5] analyzes the correlation of chunks in the divided echo image to predict echoes. Optical-flow [6], [7] establishes spatio-temporal relationships between adjacent frames to capture motion information. Multi-scale optical flow analysis of variance (MOVA) [6] applies multiple scale constraints to stationary the motion field and reduce the extrapolation discontinuity. Real-time Optical flow by Variational methods for Echoes of Radar (ROVER) [7] enhances the continuity by preprocessing the radar reflectance of aquatic animals before applying MOVA. Semi-Lagrangian advection can be used for future extrapolation after implementing optical flow [8], [9].

Numerical models have a drawback in that they estimate the motion of echoes based on only a few observations, which makes it difficult to establish the temporal correlation among them. Furthermore, optical flow-based approaches rely on the assumption of constant brightness, which is easily violated in the motion pattern of radar echoes. The assumption of no growth or decay of precipitation during semi-Lagrangian extrapolation (known as Lagrangian persistence) is inaccurate.

### B. DL-based Radar Echo Extrapolation

Numerous deep learning (DL)-based models have been developed for spatiotemporal forecasting of radar echoes. These data-driven techniques use powerful nonlinear fitting units to abstract complex spatiotemporal representations among echo motion processes without considering potential physical constraints in the atmosphere. The two typical strategies for echo extrapolation are the convolutional neural network (CNN)-based and recurrent neural network (RNN)-based approaches.

CNN-based approaches simultaneously process spatial and temporal features in the echo sequence by using convolution kernels to directly learn the translation mode from historical observations to future representation. Ayzel et al. [20] used an all-CNN model that performs comparably to the optical flow algorithm. Agrawal et al. [21] employed a U-Net [28] that fuses features from abstract to concrete levels to predict echoes, outperforming optical flow, persistence, and high-resolution rapid refresh (HRRR) numerical models in 1-hour forecasting. Song et al. [22] proposed a modified U-Net based on ResNet [29] and attention module [30] to provide a more accurate representation of echo details. Li et al. [31] incorporated satellite brightness as auxiliary information inputs to help predict echo intensity using a U-Net model. Castro et al. [23] proposed a 3D convolutional layer to address spatiotemporal causal constraints in weather forecasting.

The RNN-based approach uses recurrent connections to establish temporal correlations among echo motion processes. Shi et al. [12] introduced a novel long short-term memory (LSTM) with conventional operation to model echo motion patterns for spatially adjacent regions. Wang et al. [18] proposed a non-stationary learning unit to improve the learning and perception of long-term echo variations. S nderby et al. [24] built a model for predicting high-resolution precipitation using ConvLSTM relying on multiple data sources, including echo intensity, topography, and satellite images. Kloczek et al. [25] combined ConvLSTM with a numerical model to improve

the forecasting accuracy of long-term participation. Jing et al. [26] used a coarse-to-fine recurrent strategy to improve RNN models' long-term inference performance.

Although CNN- and RNN-based approaches are useful in learning limited representations of echoes from historical observations and period-limited temporal correlations, they have limitations. These methods are vulnerable to weak sparse echo features and non-stationary weather processes, which may affect their reliability. Additionally, the rapid decay of echo refinement and prediction accuracy with increasing extrapolation time is a significant drawback of run-based methods, which may limit their availability.

### C. Vision Transformers (ViTs)

The Transformer architecture [32] has brought a revolution to the field of natural language processing (NLP) by employing self-attention as the sole mechanism for handling long-term dependencies in sequential data. This success has inspired researchers to propose Vision Transformers (ViTs) [33] as a means of encoding image token sequences. However, to enhance the applicability and performance of transformers in image data processing, several approaches have been proposed, some of which come at the cost of increased computational complexity. For example, Dosovitskiy et al. [33] used patch segmentation to divide the original image into several small patches and extract tokens separately, while Touvron et al. [34] improved the attention mechanism by introducing formaldehyde and class-specific attention. Similarly, Fan et al. [35] devised a multiscale ViT structure, and Zhou et al. [36] re-generated attention maps to promote diversity at various levels of representation. In this paper, we present a computational method for attentional computation that is efficient and has low computational complexity. Our proposed method models the global and local relationships of the input feature maps in the ViT. Our goal is to achieve state-of-the-art performance while keeping computational costs to a minimum.

## III. TEMPORAL-SPATIAL PARALLEL TRANSFORMER (TEMPEE)

Fig. 1 presents the architecture of the proposed Temporal-Spatial Parallel Transformer, *TempEE*. Unlike auto-regression-based RNNs and Transformers that can suffer from the issue of cumulative error spreading during inference, the proposed *TempEE* uses a one-step forward extrapolation mechanism to address this issue. The *TempEE* model comprises three main components, namely the Temporal Encoder (TE), Spatial Encoder (SE), and Temporal-Spatial Decoder (TSD). The TE and SE extract intricate spatio-temporal correlations of the echo features in the temporal and spatial dimensions, respectively. The TSD uses the concatenated spatio-temporal features to decode and predict future echoes. The succeeding sections provide a detailed description of each of these modules.

### A. Temporal Encoder (TE)

Our proposed Temporal Transformer Encoder (TE), is designed to accurately forecast echo images by effectively capturing their temporal correlations despite being low-resourced.

As illustrated in Figure 2, the TE leverages a Temporal Multi-Level Multi-Head Self-Attention (Temporal MHSA) mechanism that employs weight-sharing and local Temporal MHSA modules to extract temporal correlation information from the echo feature along the timeline. The core of our TE model is the Temporal MHSA mechanism, which allows for uninterrupted learning and reshaping of local parameters to capture the degree of temporal correlation among the echo images. Our proposed TE model guarantees reliable forecasting performance while remaining resource-efficient.

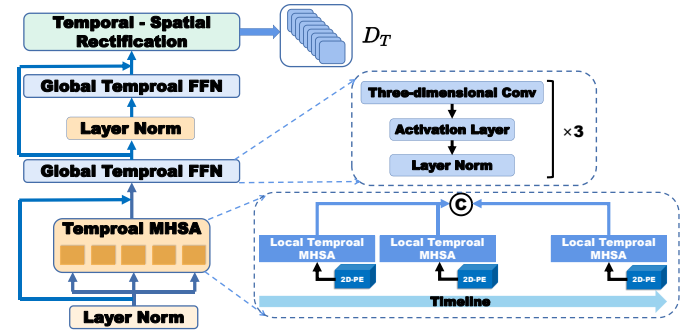


Fig. 2. Architecture of the Temporal Transformer Encoder (TE), which consists of two layer norm modules, two global Temporal FFN modules, Temporal Multi-Level Multi-Head Self-attention (Temporal MHSA), and Temporal-Spatial Rectification.

a) *MHSA in TempEE*: The success of the Transformer model largely depends on its Multi-Head Self-Attention (MHSA) mechanism, which is effective and efficient in capturing complex dependencies in input data. However, this mechanism can also cause high computational complexity, leading to slower inference speed. This issue is particularly troublesome in real-time weather forecasting applications that rely on radar echo extrapolation. To address this challenge and ensure fast inference speed without compromising accuracy, we propose a novel approach called Multi-Level Multi-Head Self-Attention. This approach is designed to optimize the trade-off between complexity and accuracy.

The computation steps of the MHSA are introduced in the follows. First, given the feature map  $\mathbf{I}_F \in \mathbb{R}^{c \times h \times w}$ , where  $c$ ,  $h$ , and  $w$  represent the channels, height, and width, respectively,  $\mathbf{I}_F$  is reshaped before being fed into the attention module to obtain the query  $\mathbf{Q}$ , key  $\mathbf{K}$ , and value  $\mathbf{V}$  matrices. Specifically, we reshape  $\mathbf{I}_F$  to  $\mathbf{I}_F \in \mathbb{R}^{c \times (h \times w)}$ , and obtain:

$$\mathbf{Q} = W^q \mathbf{I}_F, \mathbf{K} = W^k \mathbf{I}_F, \mathbf{V} = W^v \mathbf{I}_F, \quad (1)$$

where the  $W^q$ ,  $W^k$ , and  $W^v$  denotes the trainable weight matrices for  $\mathbf{Q}$ ,  $\mathbf{K}$ , and  $\mathbf{V}$ , respectively. Next, we compute the attention matrix from  $\mathbf{Q}$  and  $\mathbf{K}$  using the softmax function, resulting in:

$$\mathbf{Att} = \text{Softmax}(\mathbf{QK}^T / \sqrt{d}), \quad (2)$$

where the  $\sqrt{d}$  is an approximate normalization constant. The output is then computed by taking the matrix product of  $\mathbf{Att}$  and  $\mathbf{V}$ , yielding:

$$\mathbf{A} = \mathbf{AttV}. \quad (3)$$

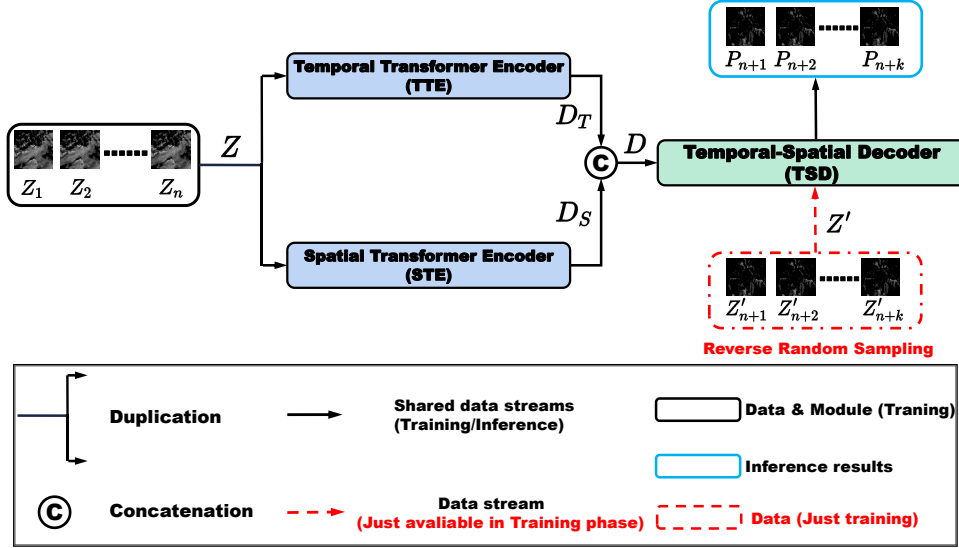


Fig. 1. Architecture of the proposed Temporal-Spatial Parallel Transformer for radar echo extrapolation, which consist of Temporal Transformer Encoder (TE), Spatial Transformer Encoder (SE), and Temporal-Spatial Decoder (TSD) in which the Reverse Random Sampling is utilized.

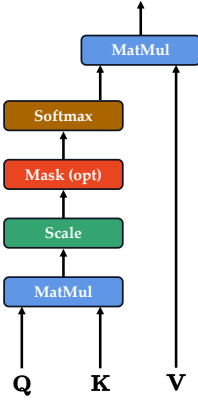


Fig. 3. Architecture of the proposed Multi-Level Multi-Head Self-Attention.

This process involves first computing the similarity between each pair of tokens using the product  $\mathbf{Q}\mathbf{K}^T$ , and then deriving each new token by combining all tokens based on their similarity. Finally, we compute the attention's output by adding a residual connection, which is expressed as

$$\mathbf{I}_F \in \mathbb{R}^{c \times (h \times w)} \xrightarrow{\text{reshape}} \mathbf{I}_F \in \mathbb{R}^{c \times h \times w}, \quad (4)$$

$$\mathbf{I}_o = \mathbf{A}\mathbf{W}^p, \quad (5)$$

in which the  $\mathbf{W}^p$  is a trainable matrix that shape is  $\mathbf{W}^p \in \mathbb{R}^{c \times c}$  for feature projection.

Since this attention module contains  $N$  heads internally (i.e.,  $N$ -heads Self-Attention), its final attention output is summed over the channel dimensions according to the results of Eq. (9). The computation complexity of MHSA can be inferred from Eqs. (4)-(9), resulting in

$$\Omega(\text{MHSA}) = 2ch^2w^2 + 3hwc^2. \quad (6)$$

Additionally, the space complexity includes the term  $O(h^2w^2)$ , indicating that memory consumption could become

very large when the input is high-resolution ( $h \times w$ ). This limits the application of the MHSA module to radar extrapolation tasks that place demands on fast training and inference.

b) *Global Temporal FFN*: The Global Temporal FFN is a normal feature extrapolation network that integrates features from the last operation. This module consists of three [Layer Norm-Activation Layer-3-D Convolution] sequences. In our work, the activation layers is based on *ReLU*, and a single part of Global Temporal FFN ( $GTF_i$ ) can be formulated as:

$$GTF_i(\cdot) = \text{Conv}(\text{ReLU}(\text{Layer Norm}(\cdot))). \quad (7)$$

c) *Temporal-Spatial Rectification*: The proposed TE mainly focuses on establishing temporal correlations between echo images and the timeline. The Temporal-Spatial Rectification aims to rectify the spatial and temporal echo features before entering the encoder module with SE. It serves to combine the temporal and spatial features for better analysis. The process can be expressed as  $\mathbf{I} \in \mathbb{R}^{c \times w \times h \times t} \rightarrow \mathbf{I} \in \mathbb{R}^{(c \times t) \times w}$ , where  $t$  is the number of time step.

### B. Spatial Encoder (SE)

The Spatial Encoder (SE) is designed to work in parallel with the Temporal Transformer Encoder (TE) to create contextual local-global feature correlations in echo images. Rather than attempting to challenge the understanding of forward temporal correlations along the timeline, the SE focuses on constructing these correlations. The overall structure of the SE is illustrated in Fig. 4. Notably, the Spatial MHSA eliminates the weight-sharing MHSA along the timeline, while the Temporal MHSA maintains consistency in all other aspects. In addition, the convolutional module of Global Spatial FFN is replaced with 2-D Convolution units contrast to Global Temporal FFN, and a single part of Global Spatial FFN ( $GSF_i$ ) can be formulated as:

$$GSF_i(\cdot) = \text{Conv}(\text{ReLU}(\text{Layer Norm}(\cdot))). \quad (8)$$

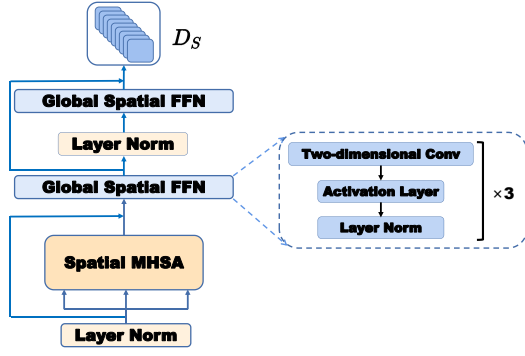


Fig. 4. Architecture of the Spatial Encoder (SE), which consists of two layer norm modules, two global Spatial FFN modules, and Spatial MHSA.

### C. Temporal-Spatial Decoder (TSD)

The Temporal-Spatial Decoder (TSD) represents a significant departure from the conventional Transformer Decoder's auto-regression mechanism for forecasting. Instead, it utilizes a Multi-level Spatio-Temporal Attention (MSTA) and a reverse random sampling strategy to construct contextual relationships among sequences, resulting in a one-step forecasting mode. This approach addresses the problem of feature dissipation, which is commonly observed in auto-regressive processes. The TSD's structure is illustrated in Figure 5. In the following section, we provide a theoretical analysis and design of the MSTA. In addition, the reverse random sampling strategy is refer to Ref. [37].

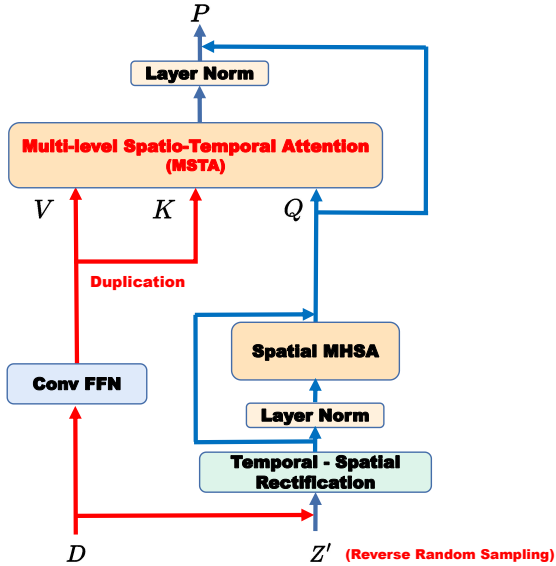


Fig. 5. Architecture of the Temporal-Spatial Decoder (TSD), which consists of a Conv FFN, a Temporal-Spatial Rectification, two Layer Norm modules, and Multi-level Spatio-Temporal Attention (MSTA).

a) *Multi-level Spatio-Temporal Attention (MSTA)*: Fig.6 depicts the architecture of the Multi-scale and multi-level Spatio-Temporal Attention (MSTA) method. Unlike the Multi-Head Self-Attention (MHSA) method shown in Fig.3, which computes the attention score for the entire image simultaneously, MSTA processes the input echo image using a novel approach. MSTA divides the image into multiple progressively

refined levels, with only a limited number of tokens involved in each computation. This approach allows MSTA to analyze fine-grained feature regions, such as weak intensity areas and typhoon eyes, while simultaneously capturing global-local information in the decoding process.

To achieve this, MSTA divides the input echo image  $\mathbf{I}_F \in \mathbb{R}^{c \times h \times w}$  into smaller grids before computing the attention score. Each grid is represented as  $\mathbf{G} \in \mathbb{R}^{g \times g}$ , and the input feature map is reshaped accordingly. This strategy enables MSTA to concentrate on specific image regions instead of processing the whole image simultaneously.

The transformation process from  $\mathbf{I}_F$  to  $\mathbf{I}_{F1}$  is as follows:  $\mathbf{I}_F \in \mathbb{R}^{c \times h \times w}$  is divided into  $\mathbf{I}_{F1} \in \mathbb{R}^{c \times (\frac{h}{g} \times g) \times (\frac{w}{g} \times g)}$  small grids, which are further reshaped to  $\mathbf{I}_{F1} \in \mathbb{R}^{c \times (\frac{h}{g} \times \frac{w}{g}) \times (g \times g)}$ .

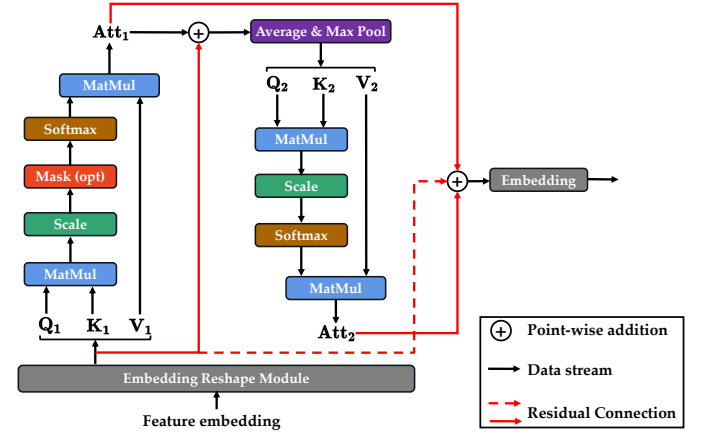


Fig. 6. Architecture of the proposed Multi-Level Multi-Head Self-Attention.

The query, key, and value of this level can be obtained by

$$\mathbf{Q}_1 = \mathbf{I}_{F1} \mathbf{W}_1^q, \mathbf{K}_1 = \mathbf{I}_{F1} \mathbf{W}_1^k, \mathbf{V}_1 = \mathbf{I}_{F1} \mathbf{W}_1^v, \quad (9)$$

where  $\mathbf{W}_1^q$ ,  $\mathbf{W}_1^k$ , and  $\mathbf{W}_1^v$  are trainable weight matrices that is  $\mathbf{W}_1^q \in \mathbb{R}^{c \times c}$ ,  $\mathbf{W}_1^k \in \mathbb{R}^{c \times c}$ , and  $\mathbf{W}_1^v \in \mathbb{R}^{c \times c}$ , respectively. Then, the local attention of this level can be generated by

$$\mathbf{Att}_1 = \text{Softmax}(\mathbf{Q}_1 \mathbf{K}_1^T / \sqrt{d}) \mathbf{V}_1, \quad (10)$$

The input attention map  $\mathbf{Att}_1$  is first reshaped to match the shape of the input image  $\mathbf{I}_F$  before computing the subsequent level of local attention. A residual connection is then applied between this local attention map and the input image, resulting in the modified attention map  $\mathbf{Att}_1$  given by:

$$\begin{aligned} \mathbf{Att}_1 \in \mathbb{R}^{c \times (\frac{h}{g} \times \frac{w}{g}) \times (g \times g)} &\rightarrow \mathbf{Att}_1 \in \mathbb{R}^{c \times (\frac{h}{g} \times g) \times (\frac{w}{g} \times g)} \\ &\rightarrow \mathbf{Att}_1 \in \mathbb{R}^{c \times h \times w}, \end{aligned} \quad (11)$$

$$\mathbf{Att}_1 = \mathbf{Att}_1 + \mathbf{I}_F. \quad (12)$$

Compared to the conventional MHSA, which operates directly on  $h$  or  $w$ ,  $\mathbf{Att}_1$  performs attention on a smaller  $g \times g$  grid, significantly reducing its space complexity. After entering the next computational level,  $\mathbf{Att}_1$  is downsampled by pooling to  $g'$ . Each  $g' \times g'$  small grid  $\mathbf{G}' \in \mathbb{R}^{g' \times g'}$  is then treated as a token in the calculation. The process is expressed as:

$$\mathbf{Att}'_1 = \frac{1}{2} [\alpha \times \text{MaxPool}_{g'}(\mathbf{Att}_1) + \beta \times \text{AvePool}_{g'}(\mathbf{Att}_1)], \quad (13)$$

where  $\text{MaxPool}g'(x)$  and  $\text{AvePool}g'(x)$  downsample the input feature map by  $g'$  using max pooling and average pooling with filter size and stride of  $g'$ , respectively. The control coefficients  $\alpha$  and  $\beta$  are importance coefficients. The resulting  $\text{Att}'_1$  has shape  $\text{Att}'_1 \in \mathbb{R}^{c \times \frac{h}{g'} \times \frac{w}{g'}}$ . The token size  $(\frac{h}{g'} \times \frac{w}{g'})$  can be obtained from the reshaped  $\text{Att}'_1$ :

$$\text{Att}'_1 \in \mathbb{R}^{c \times \frac{h}{g'} \times \frac{w}{g'}} \rightarrow \text{Att}'_1 \in \mathbb{R}^{c \times (\frac{h}{g'} \times \frac{w}{g'})}. \quad (14)$$

At this level,  $\text{Att}'_1$  computes the query, key, and value, which are denoted as  $\mathbf{Q}_2$ ,  $\mathbf{K}_2$ , and  $\mathbf{V}_2$ , respectively:

$$\mathbf{Q}_2 = \text{Att}'_1 \mathbf{W}_2^q, \quad \mathbf{K}_2 = \text{Att}'_1 \mathbf{W}_2^k, \quad \mathbf{V}_2 = \text{Att}'_1 \mathbf{W}_2^v, \quad (15)$$

where  $\mathbf{W}_2^q$ ,  $\mathbf{W}_2^k$ , and  $\mathbf{W}_2^v$  are trainable weight matrices with dimensions  $\mathbf{W}_2^q \in \mathbb{R}^{c \times c}$ ,  $\mathbf{W}_2^k \in \mathbb{R}^{c \times c}$ , and  $\mathbf{W}_2^v \in \mathbb{R}^{c \times c}$ , respectively. The local attention  $\text{Att}_2$  can be computed as follows:

$$\text{Att}_2 = \text{Softmax}(\mathbf{Q}_2 \mathbf{K}_2^T / \sqrt{d}) \mathbf{V}_2, \quad (16)$$

The final output of the MSTA is computed by the reshaping operation and a residual connection:

$$\text{Att}_2 \in \mathbb{R}^{c \times (h \times w)} \rightarrow \text{Att}_2 \in \mathbb{R}^{c \times h \times w}, \quad (17)$$

$$\text{MSTA}(\mathbf{I}_F) = (\text{Att}_1 + \text{Att}_2) \mathbf{W}^m \mathbf{W}^n + \mathbf{I}_F, \quad (18)$$

where  $\mathbf{W}^m$  and  $\mathbf{W}^n$  are trainable weight matrices. By fusing different levels of attention outputs, the proposed MMSA has strong local and global feature modeling capabilities. The computational complexity of MMSA can be computed as follows:

$$\Omega(\text{MSTA}) = chw(2g'^2 + 4c) + \frac{2chw}{g'^2}(c + hw), \quad (19)$$

which implies that the computational complexity is reduced from  $O(h^2w^2)$  to  $O(hwg^2 + \frac{h^2w^2}{g'^2})$ . The computation complexity of Multi-Head Self-Attention can be expressed:

$$\Omega(\text{MHSA}) = 2ch^2w^2 + 3hwc^2. \quad (20)$$

According to the Eq. (13), the comparison of computational complexity between our proposed MSTA and the conventional MHSA is cleared. Suppose that the echo image input is  $360 \times 360 \times 3$ , and  $g'$  in MSTA is 2, the computational parameters of conventional MHSA and our MSTA are:

$$\begin{aligned} P_{\text{MHSA}} &= 2 * 3 * 360^4 + 3 * 360^2 * 3^2 = 100,780,459,200, \\ P_{\text{MSTA}}^{g'=2} &= 3 * 360^2 * (2^3 + 4 * 3) + \frac{2 * 3 * 360^2}{2^2} * (3 + 360^2) \\ &= 25,202,599,200, \end{aligned} \quad (21)$$

This means that our MSTA pays only a quarter of the computational cost of the conventional MHSA when  $g' = 2$ .

## IV. EXPERIMENT

### A. Dataset and Pre-processing

Radar echo images were collected from three independent radars which were located in Guangzhou, Zhaoqing, and Zhuhai, Guangdong Province, China. All radar echoes are centered in Foshan, Guangdong Province, China, and the radiation

area is  $360\text{km} \times 360\text{km}$ , as shown in Fig. 7. These radars echoes are Constant Altitude Plan Position Indicator (CAPPI) that are collected every six-minute intervals periodically at 1,000 meters.



Fig. 7. Location and radiation range of radar: (a) Guangzhou; (b) Zhaoqing; (c) Zhuhai. The lower red triangle represents the position of the radar, and the red circle represents the radiation range.

Fusion of the echo images of the three radars is an essential step in the data preprocessing, ensuring that the area covered by the echo distribution of the network input and output is consistent. This step can be formulated as Eq.(22).

$$R_{(x,y)} = \text{Max}[GZ_{(x,y)}, ZQ_{(x,y)}, ZH_{(x,y)}] \quad (22)$$

where  $R_{(x,y)}$ ,  $GZ_{(x,y)}$ ,  $ZQ_{(x,y)}$  and  $ZH_{(x,y)}$  represent the intensity of the final dataset radar echo, Guangzhou radar echo, Zhaoqing radar echo, and Zhuhai radar echo at point  $(x, y)$  respectively.  $x, y$  are considered integers were belonging to the interval  $[0, 360]$  because the size of the radar echo image is  $360 \times 360$ . Note that they will be resized to  $224 \times 224$  during the training. Some examples are shown in Fig. 8.

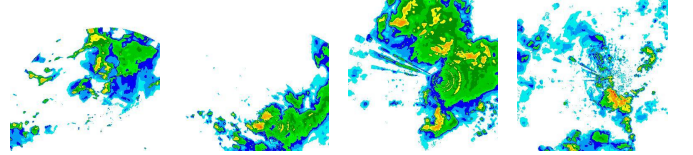


Fig. 8. Radar echo image examples of Foshan Dataset.

### B. Baseline

We introduce four baseline models for DL-based radar extrapolation to demonstrate the effectiveness of the proposed *TempEE*: MIM, PredRNN, PredRNN++, and CMS.

**MIM**: a new approach for spatiotemporal prediction using Memory In Memory (MIM) networks, which utilize differential signals to model non-stationary and approximately stationary properties [18].

**PredRNN**: a recurrent network that models visual dynamics with compositional subsystems and achieves highly competitive results on five datasets for spatiotemporal sequence predictive learning. [16], [37].

**PredRNN++**: an improved version of the PredRNN model, which includes two additional components: a spatial attention mechanism and a progressive growing mechanism [17].

**CMS**: a novel approach to spatiotemporal predictive learning that focuses on context correlations and multi-scale spatiotemporal flow using two elaborately designed blocks: Context Embedding and Spatiotemporal Expression [19].

### C. Experimental Setup

During the experiments, all radar echo maps were resized to a dimension of  $192 \times 192$ . To reduce computational consumption without losing features, the original echo images were chunked using the patch operation with a patch value of 12. We used AdamW optimizer with a WarmUp mechanism to prevent the initial learning rate from being too large, which could lead to unstable training. This mechanism, which gradually increases the learning rate from a smaller value to a more significant value at the beginning of training until reaching a preset maximum learning rate, is known as the WarmUp mechanism.

$$lr_t = \frac{k^{d_{max}}}{\sqrt{d_t}} \times \min\left(\frac{t}{w}, \sqrt{t}\right) \quad (23)$$

where  $lr_t$  denotes the learning rate of the  $t$ th step,  $d_t$  denotes the hidden layer dimension of the  $t$ th step,  $d_{max}$  denotes the maximum dimension,  $k$  denotes a constant, and  $w$  denotes the number of WarmUp steps.

To enhance the model's training effectiveness, a learning rate Cosine decay operation is utilized at the end of the WarmUp phase. This ensures that the learning rate reduces stationaryly throughout the training process and prevents the problem of the rate decreasing too fast, causing unstable training. Moreover, Cosine decay also permits the model to maintain a smaller learning rate in later stages of training, facilitating better exploration of the parameter space and mitigating overfitting. The expression of this operation is as follows:

$$lr_t = \frac{1}{2} \left(1 + \cos\left(\frac{T_{cur}}{T_{max}}\pi\right)\right) \times lr_{max}, \quad (24)$$

where  $lr_t$  denotes the learning rate of the  $t$ -th step,  $T_{cur}$  denotes the the current step,  $T_{max}$  denotes the total number of steps, and  $lr_{max}$  denotes the maximum learning rate.

### D. Performance Evaluation Metric

*a) Image-based Metric:* The Mean Squared Error (MSE) measures the average squared difference between the original image and the reconstructed image. A lower MSE value indicates better image quality, and the function of MSE can be expressed as :

$$\mathcal{L} = \frac{1}{Q \cdot mn} \sum_{T=0}^Q \sum_{i=0}^m \sum_{j=0}^n [I_{i,j} - K_{i,j}]^2, \quad (25)$$

where the  $I$  is ground truth of echo image and  $K$  is the extrapolation,  $Q$  denotes the extrapolation period,  $m$  and  $n$  is the echo image's row and column, respectively.

Peak Signal-to-Noise Ratio (PSNR) is a commonly used measure in image reconstruction research. It represents the ratio between the maximum possible power of a signal and the power of corrupting noise that affects the fidelity of the signal's representation. PSNR is expressed in decibels (dB), and a larger value indicates better image quality.

$$\text{PSNR} = 10 \log_{10} \left( \frac{MAX_I^2}{\text{MSE}} \right), \quad (26)$$

where  $MAX_I$  indicates the maximum value of the pixel, usually 255.

The Structural Similarity Index (SSIM) measures the similarity between two images by comparing their luminance, contrast, and structural information. SSIM compares the local image structures between the original and the reconstructed images, rather than just comparing the pixel values. A higher SSIM value indicates better image quality.

$$\text{SSIM}(x, y) = \frac{(2\mu_x\mu_y + c_1)(2\sigma_{xy} + c_2)}{(\mu_x^2 + \mu_y^2 + c_1)(\sigma_x^2 + \sigma_y^2 + c_2)}, \quad (27)$$

where  $\mu_x$  and  $\mu_y$  are the means of  $x$  and  $y$ , respectively,  $\sigma_x^2$  and  $\sigma_y^2$  are the variances of  $x$  and  $y$ , respectively,  $\sigma_{xy}$  is the covariance of  $x$  and  $y$ , and  $c_1$  and  $c_2$  are two constants.

Learned Perceptual Image Patch Similarity (LPIPS) utilizes learned features from neural networks to compute the perceptual similarity between two images. LPIPS is based on the hierarchical processing of visual information in the human visual system, starting with lower-level features such as edges and textures and progressing to higher-level features associated with object recognition. LPIPS computes the distance between the feature representations of the two images, whose features are learned from a dataset of images. A lower LPIPS value indicates greater perceptual similarity between the images.

$$\text{LPIPS}(x, y) = \sum_{i=1}^N w_i \cdot \|\phi_i(x) - \phi_i(y)\|_2, \quad (28)$$

where  $\phi_i(\cdot)$  denotes the feature map output from the  $i$ th layer of the model,  $w_i$  denotes the weight of the  $i$ th layer feature map, and  $N$  denotes the number of layers of the model.

*b) Meteorological Evaluation Metric:* The study employed commonly used evaluation metrics in the field of meteorology to assess model performance synthetically. These metrics comprised the probability of detection (POD), false alarm rate (FAR), and critical success index (CSI). These metrics offer a measure of the accuracy of model predictions. A lower FAR value indicates a larger discrepancy between the extrapolated echo and the ground truth. Larger values of CSI, POD, and accuracy (ACC) demonstrate a closer correlation between the predicted results and ground truth. In an ideal scenario of a perfect forecast, the FAR would be zero, and the CSI, POD, and ACC would all be equal to one.

We calculated these metrics based on different rainfall intensities, ranging from probable precipitation (0.05 mm/h) to 40 mm/h, estimated from the radar echo reflectance using the Z-R relationship [38]. The threshold determines whether a certain pixel value on the radar echo image becomes 0/1 based on the echo intensity in the area represented by the point. The parameters True Positive (hits), Fake Negative (misses), Fake Positive (false alarms), and True Negative (correct negatives) can be calculated by comparing predicted results to ground truth. The meteorological evaluation metrics were formulated as Eqs. (29) to (31).

$$\text{POD} = \frac{\text{TP}}{\text{TP} + \text{FN}}, \quad (29)$$

$$\text{FAR} = \frac{\text{FP}}{\text{TP} + \text{FP}}, \quad (30)$$

$$\text{CSI} = \frac{\text{TP}}{\text{TP} + \text{FN} + \text{FP}}, \quad (31)$$

$$\text{ETS} = \frac{\text{TP}}{\text{TP} + \text{FN} + \text{FP} - \text{TN}}. \quad (32)$$

### E. Experiment Results

To verify the effectiveness and superiority of the proposed *TempEE* in radar echo extrapolation tasks, a series of experiments were conducted and they were analyzed quantitatively and qualitatively.

a) *Image-based Performance Evaluation*: The task of radar echo extrapolation involves using historical observations to predict future radar representations in a temporal-spatial manner. In this study, we propose a novel approach named *TempEE*, and evaluate its effectiveness in generating high-quality radar images compared to baseline models. To assess the validity and superiority of *TempEE*, we utilized several image-based metrics, including PSNR, SSIM, MSE, and LPIPS, to perform a comprehensive evaluation. The performance comparison between *TempEE* and the baseline models is presented in Table I. The results demonstrate that *TempEE* significantly outperforms the other baseline models, indicating that our proposed approach is capable of achieving superior accuracy and image quality for temporal-spatial image generation in radar echo extrapolation.

TABLE I  
PERFORMANCE COMPARISON OF THE PROPOSED *TempEE* AND BASELINE UNDER METRICS ON TEMPORAL-SPATIAL IMAGE GENERATION, AND  $\uparrow$  AND  $\downarrow$  REPRESENT THE HIGHER/LOWER THE METRIC, THE BETTER/POORER THE PERFORMANCE, THE **BOLD** MEANS THE OPTIMAL.

Model	PSNR $\uparrow$	SSIM $\uparrow$	MSE $\downarrow$	LPIPS $\downarrow$
PredRNN	281.61	0.498	309.17	5.27
PredRNN++	274.84	0.515	301.93	4.188
CMS	277.26	0.509	282.82	4.102
MIM	277.37	0.52	249.16	4.232
<i>TempEE</i> (Ours)	<b>389.14</b>	<b>0.876</b>	<b>29.82</b>	<b>1.058</b>

b) *Quantitative Performance Evaluation of Perception Forecasting*: The performance of the proposed *TempEE* model was evaluated under varying rainfall conditions using four rainfall forecast-related assessment metrics: CSI, FAR, FAR, and POD. The model's performance was compared with a baseline model using the complete test dataset, and the results were analyzed and presented in Table II.

The analysis shows that the *TempEE* model consistently outperforms the baseline model across different rainfall intensities. Specifically, as rainfall intensity increases, the *TempEE* model exhibits the lowest decay span for each meteorological indicator, indicating a near unit-by-unit decrease in *TempEE* of about 0.13 on CSI for rainfall intensity intervals ranging from 10 mm/h to 30 mm/h. In comparison, the corresponding figures for other models, such as PredRNN, PredRNN++, CMS, and MIM, are 0.16, 0.20, 0.18, and 0.18, respectively. These results suggest that the proposed *TempEE* model performs better than the baseline models in the overall extrapolation process. This means that the proposed *TempEE* model is highly effective in predicting rainfall under different conditions, as demonstrated

by its superior performance in comparison to the baseline models across all rainfall intensities.

One potential drawback of extrapolation in radar algorithms is the accumulation of errors, which can significantly degrade the accuracy and quality of echo in long-term extrapolation. To assess the effectiveness of the proposed *TempEE* in long sequence extrapolation, we compare its performance to a baseline model over time at rainfall intensities of 5 mm/h, 10 mm/h, 20 mm/h, 30 mm/h, and 40 mm/h in Fig.9, Fig.10, Fig.11, Fig.12, and Fig.13, respectively. Our analysis indicates that: 1) *TempEE* outperforms baseline models across different evaluation metrics and rainfall intensities; 2) *TempEE* can maintain relatively stationary performance in long extrapolation processes compared to other models that suffer from the decay of extrapolation accuracy over time. The only exceptions are the large fluctuations observed at the first time node (0 ~ 6 min) and the last time node (114 ~ 120 min), which are caused by the out back-sampling strategy that mixes prior knowledge at the first time node and the last point of time node. This suggests that *TempEE*'s one-forward step extrapolation is superior to conventional auto-regression mechanisms and avoids error spreading during the inference phase.

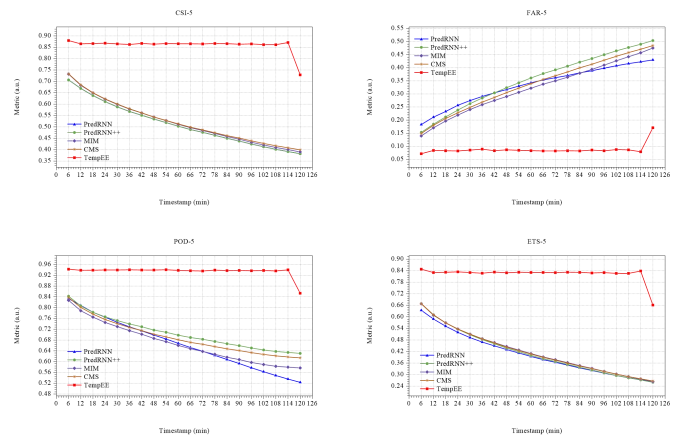


Fig. 9. Time-by-time performance comparison of the proposed *TempEE* and baseline model under precipitation forecasting-based metrics when  $\tau = 5$ .

c) *Qualitative Performance Evaluation of Perception Forecasting*: The quality of radar echo images is crucial for weather forecasters to obtain effective guidance from extrapolation models. The effectiveness and prediction accuracy of the proposed *TempEE* model were tested using four different echo motion processes from the complete test dataset. To differentiate between these processes, we categorized them into two groups: stationary and nonstationary. Moreover, based on the characteristics of the echoes, we further classified the processes into four subgroups: Sparse-Stationary (Fig.14), Dense-Stationary (Fig.15), Sparse-Nonstationary (Fig.16), and Dense-Nonstationary (Fig.17). The visualization of these model inference results demonstrated the effectiveness and superior prediction accuracy of the proposed *TempEE* model across these different echo motion processes.

### Case Study on Sparse-Stationary Motion Process



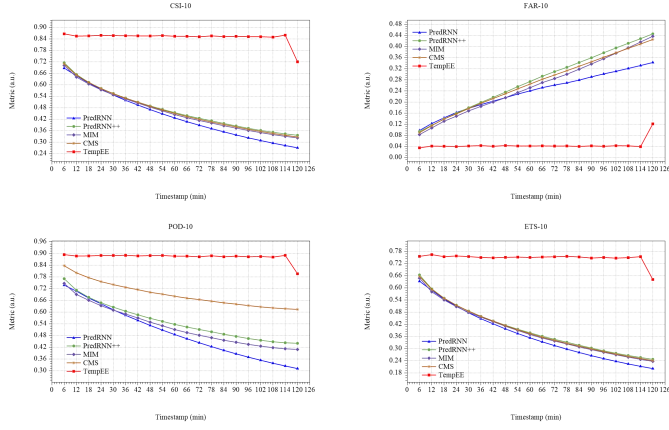


Fig. 10. Time-by-time performance comparison of the proposed *TempEE* and baseline model under precipitation forecasting-based metrics when  $\tau = 10$ .

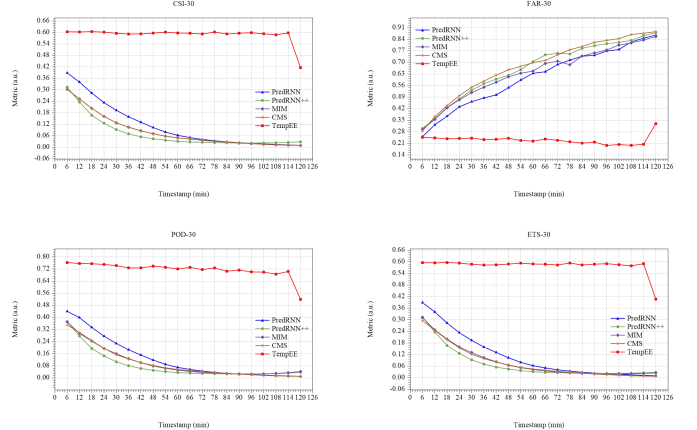


Fig. 12. Time-by-time performance comparison of the proposed *TempEE* and baseline model under precipitation forecasting-based metrics when  $\tau = 30$ .

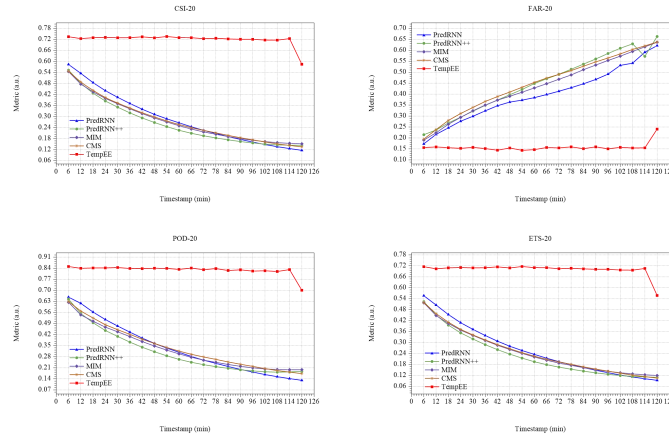


Fig. 11. Time-by-time performance comparison of the proposed *TempEE* and baseline model under precipitation forecasting-based metrics when  $\tau = 20$ .

During a two-hour sparse-stationary motion, the baseline models captured the general echo distribution, but they were unable to account for most of the sparse echo features, especially the series of sparse points in the lower right of the

echo image. Over time, these baseline models demonstrated unsatisfactory results in both echo intensity and feature distribution. On the other hand, the proposed *TempEE* model can effectively capture the fine echo features. Although there might be a few points with extrapolated intensity that are either too high or too low, its overall effect remains stable over time.

### Case Study on Dense-Stationary Motion Process

All models show the ability to capture the general motion trend of the radar echo distribution. For example, from  $T=126\text{min}$  to  $T=234\text{min}$ , the radar echo gradually moves from the left to the upper right direction, accompanied by a certain degree of radar echo dissipation. The Baseline model captures the overall motion trend, but it has difficulty accounting for the finer details present in the data. Moreover, as the extrapolation process advances, the Baseline model fails to capture the radar echo feature dissipation.

In contrast, the proposed *TempEE* model offers a more comprehensive representation of the radar echo trend during this motion, including both the overall motion trend and the trend of radar echo dissipation. Additionally, the *TempEE* model exhibits a solid ability to represent a series of isolated

TABLE II

PERFORMANCE COMPARISON BETWEEN THE PROPOSED *TempEE* AND BASELINE BASED ON PERCEPTION FORECASTING-BASED METRICS, WHERE  $\tau$  IS THE EVALUATION THRESHOLD REPRESENTING DIFFERENT RAINFALL INTENSITIES, AND  $\uparrow$  AND  $\downarrow$  REPRESENT THE HIGHER/LOWER THE METRIC, THE BETTER/POORER THE PERFORMANCE, THE **BOLD** MEANS THE OPTIMAL.

Model	CSI $\uparrow$					ETS $\uparrow$							
	Threshold	$\tau = 5$	$\tau = 10$	$\tau = 20$	$\tau = 30$	$\tau = 40$	Average	$\tau = 5$	$\tau = 10$	$\tau = 20$	$\tau = 30$	$\tau = 40$	Average
PredRNN		0.511	0.438	0.288	0.111	0.082	0.286	0.397	0.373	0.254	0.106	0.078	0.242
PredRNN++		0.522	0.469	0.261	0.071	0.044	0.273	0.413	0.398	0.259	0.067	0.061	0.240
CMS		0.524	0.466	0.282	0.084	0.051	0.271	0.411	0.391	0.272	0.119	0.049	0.248
MIM		0.521	0.45	0.276	0.086	0.054	0.277	0.419	0.400	0.246	0.077	0.069	0.242
<i>TempEE</i> (Ours)		<b>0.861</b>	<b>0.849</b>	<b>0.719</b>	<b>0.588</b>	<b>0.540</b>	<b>0.705</b>	<b>0.822</b>	<b>0.746</b>	<b>0.699</b>	<b>0.579</b>	<b>0.534</b>	<b>0.676</b>

Model	FAR $\downarrow$					POD $\uparrow$							
	Threshold	$\tau = 5$	$\tau = 10$	$\tau = 20$	$\tau = 30$	$\tau = 40$	Average	$\tau = 5$	$\tau = 10$	$\tau = 20$	$\tau = 30$	$\tau = 40$	Average
PredRNN		0.237	0.337	0.476	0.615	0.754	0.484	0.672	0.493	0.307	0.128	0.094	0.338
PredRNN++		0.279	0.329	0.464	0.599	0.734	0.481	0.681	0.551	0.332	0.083	0.051	0.340
CMS		0.268	0.337	0.449	0.643	0.772	0.494	0.691	0.541	0.339	0.108	0.05	0.346
MIM		0.261	0.323	0.433	0.638	0.707	0.472	0.709	0.527	0.328	0.101	0.062	0.345
<i>TempEE</i> (Ours)		<b>0.045</b>	<b>0.088</b>	<b>0.158</b>	<b>0.231</b>	<b>0.273</b>	<b>0.159</b>	<b>0.934</b>	<b>0.882</b>	<b>0.828</b>	<b>0.716</b>	<b>0.682</b>	<b>0.808</b>

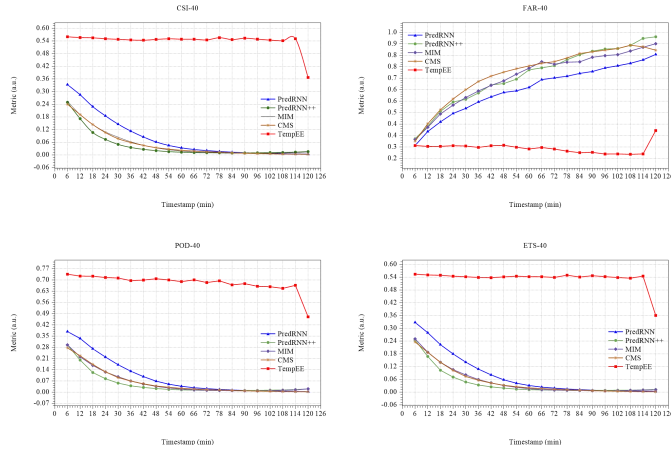


Fig. 13. Time-by-time performance comparison of the proposed *TempEE* and baseline model under precipitation forecasting-based metrics when  $\tau = 40$ .

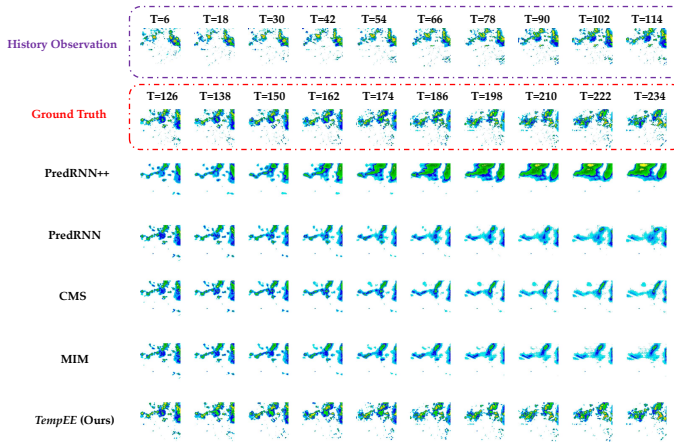


Fig. 14. Visualization of the proposed *TempEE* and baseline models during the echo Sparse-Stationary motion inference process, note that the time period actually is 6 min, but 12 min is used as the presentation period.

points below.

Overall, the *TempEE* model performs better than the Baseline model in terms of capturing the finer details of the radar echo distribution and the radar echo dissipation trend, making it a more suitable model for this application.

### Case Study on Sparse-Nonstationary Motion Process

Despite the sparse and non-stationary motion of the echo within a two-hour timeframe, the baseline model adequately characterizes the primary motion trend, which gradually moves towards the upper right, and the general shape of the echo, including the bar region on the right side. However, it cannot account for a considerable number of sparse echo features, including those that appear suddenly at  $T = 0.174$ . Additionally, the model predicts a significantly high echo intensity, indicating the need for improvement.

In contrast, the proposed *TempEE* captures the primary motion trend in regions with dense echo features and can flexibly perceive and characterize the sudden appearance of sparse echo features during the extrapolation process. Although it also encounters issues with high predicted intensity, the overall effectiveness of the *TempEE* significantly exceeds that of the

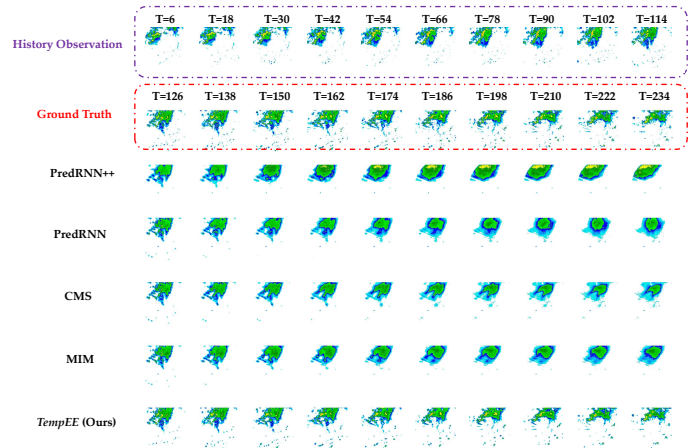


Fig. 15. Visualization of the proposed *TempEE* and baseline models during the echo Dense-Stationary motion inference process, note that the time period actually is 6 min, but 12 min is used as the presentation period.

baseline model.

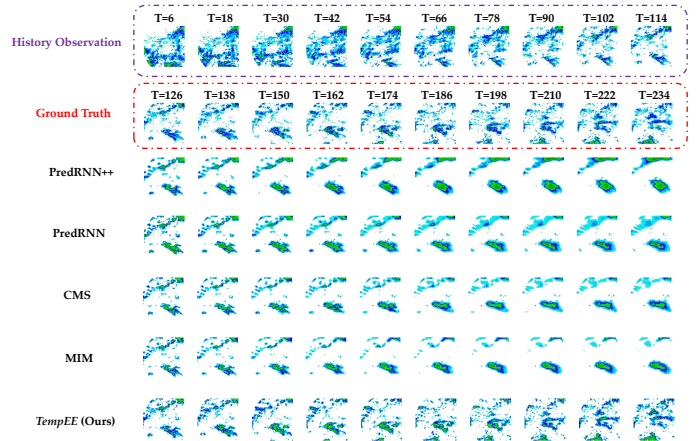


Fig. 16. Visualization of the proposed *TempEE* and baseline models during the echo Sparse-NonStationary motion inference process, note that the time period actually is 6 min, but 12 min is used as the presentation period.

**Case Study on Dense-Nonstationary Motion Process** In the presence of dense non-stationary motion and echoes occurring within 2 hours, baseline fails to capture a limited subset of echo features and exhibits a significantly lower prediction intensity. While PredRNN++ is capable of capturing the vast majority of these features, it lacks a refined feature representation. In contrast, the proposed *TempEE* demonstrates superior performance in echo feature refinement, motion and echo generation, and perception of extinction trends. Furthermore, *TempEE*'s robustness and superiority over the baseline model are evident in its ability to maintain efficacy despite the gradual dissipation of echo features over time.

The proposed *TempEE* has multiple advantages for characterizing sparse echo features and perceiving the echo generation and dissipation processes in both stationary and non-stationary motion. Additionally, it can refine echo characteristics and capture internal details based on the echoes' overall shape. Most importantly, the extrapolation effect remains robust over time, ensuring reliable analysis of long-term data.

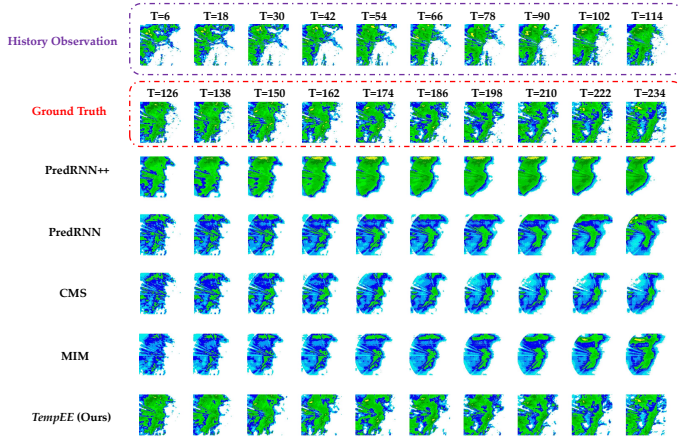


Fig. 17. Visualization of the proposed *TempEE* and baseline models during the echo Dense-Nonstationary motion inference process, note that the time period actually is 6 min, but 12 min is used as the presentation period.

Collectively, these features make *TempEE* a valuable tool for studying echo characteristics in various settings.

### F. Ablation Study

We performed a series of ablation experiments to evaluate the necessity and effectiveness of the specific modules in our proposed *TempEE*, namely TE, SE, and MSTA. Both qualitative and quantitative analyses were conducted, and the overall results of the ablation experiments are summarized in Table III. Notably, the presence of conflicting MSTA and MHSA modules means that when MSTA is removed, MHSA is utilized as its attention module in the Decoder.

Our results indicate that TE and SE are crucial for the Decoder, and there are no instances where TE/SE and MSTA are not maintained simultaneously. The removal of TE/SE leads to a significant decrease in performance, while removing MSTA while keeping TE/SE causes some degradation in the proposed *TempEE*'s performance. This suggests that MSTA possesses a robust multi-scale feature characterization capability, demonstrating the validity and necessity of TE, SE, and MSTA in our *TempEE*.

TABLE III

PERFORMANCE OF THE ABLATION STUDY IN WHICH *w/o* MEANS THAT THE PROPOSED *TempEE* WITHOUT THE CERTAIN MODULE, *w* MEANS THAT CONDUCTS THE EXPERIMENT WITH THE CERTAIN MODULE, AND  $\uparrow$  AND  $\downarrow$  REPRESENT THE HIGHER/LOWER THE METRIC, THE BETTER/POORER THE PERFORMANCE.

Model	TE	SE	MSTA	MHSA	PNSR $\uparrow$	SSIM $\uparrow$	MSE $\downarrow$	LPIS $\downarrow$
<i>TempEE</i>	<i>w</i>	<i>w</i>	<i>w</i>	<i>w/o</i>	389.14	0.876	29.82	1.058
	<i>w/o</i>	<i>w</i>	<i>w</i>	<i>w/o</i>	353.07	0.750	53.53	1.687
	<i>w</i>	<i>w/o</i>	<i>w</i>	<i>w/o</i>	361.25	0.767	46.65	1.556
	<i>w</i>	<i>w</i>	<i>w/o</i>	<i>w</i>	344.39	0.758	61.23	1.785

The ablation experiment evaluated the performance metrics of *TempEE* through image quality over time, which is illustrated in Figure 18. The results showed that all versions of *TempEE*, which did not include TE, SE, and MSTA, had a lower level of performance compared to the original *TempEE*. Nevertheless, the trend in the temporal dimension remained

relatively stable, except for an extensive decay observed at the last extrapolation time point ( $T = 240$  min) due to the proposed sampling strategy. These results further validate the superiority of the one-step forward extrapolation mechanism applied in the proposed *TempEE*. This mechanism prevents the accumulation of errors during the extrapolation process and has the potential for ultra-long period extrapolation, which is not possible with the auto-regressive extrapolation strategy.

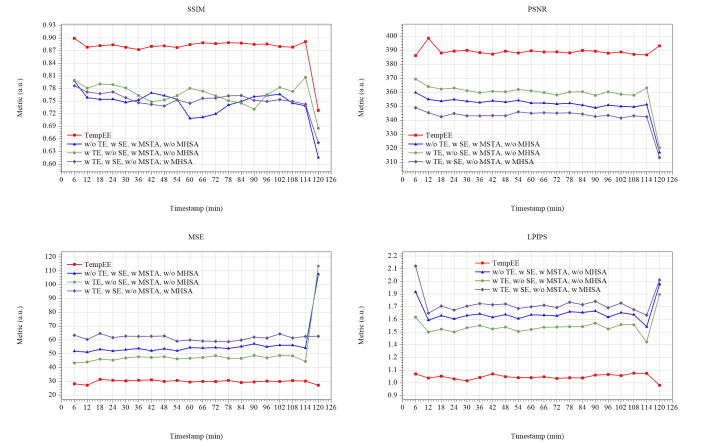


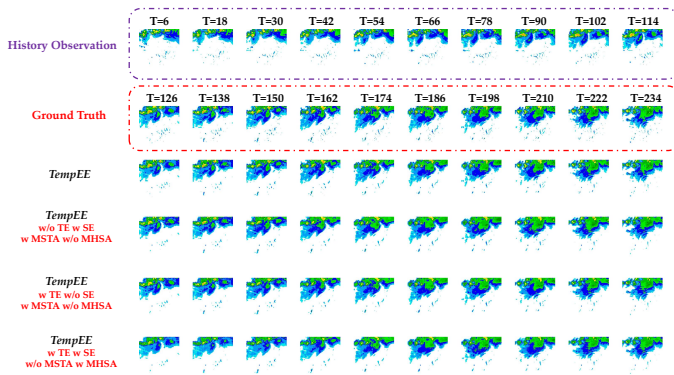
Fig. 18. Time-by-time performance comparison of the proposed *TempEE* and *TempEE*-based ablation model under image-based metrics.

The results of the ablation experiment's extrapolation for the model are presented in Figure 19, which depicts the dense and non-stationary process of echo motion with varying degrees of echo generation and extinction. The results show that the original *TempEE* has a significant impact when compared to the other ablation models. Furthermore, all models effectively capture the overall echo motion trend, sparse echo features, and abrupt changes in echo features. However, the ablation models show significant image gridding issues during the extrapolation process when compared to the original *TempEE*. As a result, the predicted echo images are not clear enough, which could marginally affect the forecast results.

The proposed one-step forward extrapolation mechanism of *TempEE* significantly outperforms the conventional auto-regressive extrapolation mechanism. It solves the fundamental issue of error accumulation in the extrapolation process of conventional extrapolation models. Furthermore, *TempEE* consistently outperforms other models in cases of stationary, non-stationary, and different echo distributions.

## V. CONCLUSION

In conclusion, this paper proposes a novel radar echo extrapolation model named *TempEE*, which offers a reliable and precise analytical support for precipitation forecasting through extrapolating radar echoes. The proposed parallel encoder structure, consisting of a Temporal Encoder and a Spatial Encoder, along with a decoder that employs attention, considers complex spatiotemporal correlations among echo distributions simultaneously. Experimental results on a real-world radar echo dataset have demonstrated the effectiveness of *TempEE* in achieving state-of-art performance with low



by the Shenzhen Hong Kong Macao science and technology plan project under Grant SGDX20210823103537035.

Fig. 19. Visualization of the the proposed *TempEE* and its ablation model’s inference process, note that the time period actually is 6 *min*, but 12 *min* is used as the presentation period.

computational cost. Moreover, extensive ablation studies confirm the necessity and efficacy of the model’s components.

However, *TempEE* still requires significant computation resources for computing attention scores, which are relatively expensive compared to convolution units. Additionally, since the real-world dataset used in this study was collected from three radars with different location information, *TempEE* does not consider geographical association during the training phase. Our future work will aim to develop a foundational model for radar echo extrapolation tasks that can incorporate geographical association while also requiring lower cost, for more general applicability.

#### ACKNOWLEDGMENTS

This work was supported in part by the National Key Research and Development Program of China for Intergovernmental Cooperation under Grant 2019YFE0110100, in part by the National Natural Science Foundation of China under Grant 42105145, in part by the Guangdong Province Natural Science Foundation under Grant 2023A1515011438, in part by the Science and technology innovation team project of Guangdong Meteorological Bureau under Grant GRMCTD202104, in part by the Innovation and Development Project of China Meteorological Administration under Grant CXFZ2022J002 and in part

TABLE IV

RESULTS OF THE ABLATION STUDY BASED ON PERCEPTION FORECASTING -BASED METRICS, WHERE  $\tau$  IS THE EVALUATION THRESHOLD REPRESENTING DIFFERENT RAINFALL INTENSITIES, AND  $\uparrow$  AND  $\downarrow$  REPRESENT THE HIGHER/LOWER THE METRIC, THE BETTER/POORER THE PERFORMANCE, AND *w* AND *w/o* DENOTES ‘WITH’ AND ‘WITHOUT’, RESPECTIVELY.

Model	CSI $\uparrow$						ETS $\uparrow$					
	$\tau = 5$	$\tau = 10$	$\tau = 20$	$\tau = 30$	$\tau = 40$	Average	$\tau = 5$	$\tau = 10$	$\tau = 20$	$\tau = 30$	$\tau = 40$	Average
<i>TempEE</i>	0.861	0.849	0.719	0.588	0.54	0.711	0.822	0.746	0.699	0.579	0.534	0.676
<i>w/o TE w/ SE w/ MSTA w/o MHSA</i>	0.794	0.773	0.655	0.48	0.422	0.625	0.74	0.734	0.625	0.461	0.406	0.593
<i>w TE w/o SE w/ MSTA w/o MHSA</i>	0.812	0.802	0.678	0.519	0.464	0.655	0.763	0.768	0.648	0.501	0.449	0.626
<i>w TE w SE w/o MSTA w/ MHSA</i>	0.782	0.758	0.604	0.382	0.32	0.569	0.727	0.709	0.573	0.365	0.306	0.536
Model	FAR $\downarrow$						POD $\uparrow$					
	$\tau = 5$	$\tau = 10$	$\tau = 20$	$\tau = 30$	$\tau = 40$	Average	$\tau = 5$	$\tau = 10$	$\tau = 20$	$\tau = 30$	$\tau = 40$	Average
<i>TempEE</i>	0.045	0.088	0.158	0.231	0.273	0.159	0.934	0.882	0.828	0.716	0.682	0.808
<i>w/o TE w/ SE w/ MSTA w/o MHSA</i>	0.77	0.149	0.186	0.271	0.315	0.200	0.913	0.841	0.756	0.571	0.513	0.719
<i>w TE w/o SE w/ MSTA w/o MHSA</i>	0.069	0.135	0.178	0.242	0.281	0.181	0.921	0.856	0.780	0.608	0.554	0.744
<i>w TE w SE w/o MSTA w/ MHSA</i>	0.072	0.144	0.150	0.220	0.255	0.168	0.892	0.799	0.661	0.414	0.349	0.623

## REFERENCES

- [1] X. Qiu and F. Zhang, "Prediction and predictability of a catastrophic local extreme precipitation event through cloud-resolving ensemble analysis and forecasting with doppler radar observations," *Science China Earth Sciences*, vol. 59, no. 3, pp. 518–532, 2016.
- [2] X. Zhao, J. Liu, D. Yu, and J. Chang, "One-day-ahead probabilistic wind speed forecast based on optimized numerical weather prediction data," *Energy Conversion and Management*, vol. 164, pp. 560–569, 2018.
- [3] C. M. Grams, L. Magnusson, and E. Madonna, "An atmospheric dynamics perspective on the amplification and propagation of forecast error in numerical weather prediction models: A case study," *Quarterly Journal of the Royal Meteorological Society*, vol. 144, no. 717, pp. 2577–2591, 2018.
- [4] M. C. V. Ramirez, H. F. de Campos Velho, and N. J. Ferreira, "Artificial neural network technique for rainfall forecasting applied to the sao paulo region," *Journal of hydrology*, vol. 301, no. 1-4, pp. 146–162, 2005.
- [5] P. Li and E. S. Lai, "Applications of radar-based nowcasting techniques for mesoscale weather forecasting in hong kong," *Meteorological Applications*, vol. 11, no. 3, pp. 253–264, 2004.
- [6] W. Wong, L. H. Yeung, Y. Wang, and M. Chen, "Towards the blending of nwp with nowcast—operation experience in b08fdp," in *WMO Symposium on Nowcasting*, vol. 30, 2009, p. 24.
- [7] W.-c. Woo and W.-k. Wong, "Operational application of optical flow techniques to radar-based rainfall nowcasting," *Atmosphere*, vol. 8, no. 3, p. 48, 2017.
- [8] U. Germann and I. Zawadzki, "Scale-dependence of the predictability of precipitation from continental radar images. part i: Description of the methodology," *Monthly Weather Review*, vol. 130, no. 12, pp. 2859–2873, 2002.
- [9] —, "Scale dependence of the predictability of precipitation from continental radar images. part ii: Probability forecasts," *Journal of Applied Meteorology*, vol. 43, no. 1, pp. 74–89, 2004.
- [10] Z. Yang, H. Wu, Q. Liu, X. Liu, Y. Zhang, and X. Cao, "A self-attention integrated spatiotemporal lstm approach to edge-radar echo extrapolation in the internet of radars," *ISA transactions*, vol. 132, pp. 155–166, 2023.
- [11] W. Fang, L. Pang, V. S. Sheng, and Q. Wang, "Stunner: Radar echo extrapolation model based on spatio-temporal fusion neural network," *IEEE Transactions on Geoscience and Remote Sensing*, 2023.
- [12] X. Shi, Z. Chen, H. Wang, D.-Y. Yeung, W.-K. Wong, and W.-c. Woo, "Convolutional lstm network: A machine learning approach for precipitation nowcasting," *Advances in neural information processing systems*, vol. 28, 2015.
- [13] Y. Hu, L. Chen, Z. Wang, X. Pan, and H. Li, "Towards a more realistic and detailed deep-learning-based radar echo extrapolation method," *Remote Sensing*, vol. 14, no. 1, p. 24, 2021.
- [14] P. Xie, X. Li, X. Ji, X. Chen, Y. Chen, J. Liu, and Y. Ye, "An energy-based generative adversarial forecaster for radar echo map extrapolation," *IEEE Geoscience and Remote Sensing Letters*, vol. 19, pp. 1–5, 2020.
- [15] J. Sun, X. Li, C. Tang, S.-H. Wang, and Y.-D. Zhang, "Mfbcnnc: Momentum factor biogeography convolutional neural network for covid-19 detection via chest x-ray images," *Knowledge-Based Systems*, vol. 232, p. 107494, 2021.
- [16] Y. Wang, M. Long, J. Wang, Z. Gao, and P. S. Yu, "Predrnn: Recurrent neural networks for predictive learning using spatiotemporal lstms," *Advances in neural information processing systems*, vol. 30, 2017.
- [17] Y. Wang, Z. Gao, M. Long, J. Wang, and S. Y. Philip, "Predrnn++: Towards a resolution of the deep-in-time dilemma in spatiotemporal predictive learning," in *International Conference on Machine Learning*. PMLR, 2018, pp. 5123–5132.
- [18] Y. Wang, J. Zhang, H. Zhu, M. Long, J. Wang, and P. S. Yu, "Memory in memory: A predictive neural network for learning higher-order non-stationarity from spatiotemporal dynamics," in *Proceedings of the IEEE/CVF Conference on Computer Vision and Pattern Recognition*, 2019, pp. 9154–9162.
- [19] Z. Chai, Z. Xu, Y. Bail, Z. Lin, and C. Yuan, "Cms-lstm: Context embedding and multi-scale spatiotemporal expression lstm for predictive learning," in *2022 IEEE International Conference on Multimedia and Expo (ICME)*. IEEE, 2022, pp. 01–06.
- [20] G. Ayzel, M. Heistermann, A. Sorokin, O. Nikitin, and O. Lukyanova, "All convolutional neural networks for radar-based precipitation nowcasting," *Procedia Computer Science*, vol. 150, pp. 186–192, 2019.
- [21] S. Agrawal, L. Barrington, C. Bromberg, J. Burge, C. Gazen, and J. Hickey, "Machine learning for precipitation nowcasting from radar images," *arXiv preprint arXiv:1912.12132*, 2019.
- [22] K. Song, G. Yang, Q. Wang, C. Xu, J. Liu, W. Liu, C. Shi, Y. Wang, G. Zhang, X. Yu *et al.*, "Deep learning prediction of incoming rainfalls: An operational service for the city of beijing china," in *2019 International Conference on Data Mining Workshops (ICDMW)*. IEEE, 2019, pp. 180–185.
- [23] R. Castro, Y. M. Souto, E. Ogasawara, F. Porto, and E. Bezerra, "Stconvs2s: Spatiotemporal convolutional sequence to sequence network for weather forecasting," *Neurocomputing*, vol. 426, pp. 285–298, 2021.
- [24] C. K. Sønderby, L. Espenholt, J. Heek, M. Dehghani, A. Oliver, T. Salimans, S. Agrawal, J. Hickey, and N. Kalchbrenner, "Metnet: A neural weather model for precipitation forecasting," *arXiv preprint arXiv:2003.12140*, 2020.
- [25] S. Klocek, H. Dong, M. Dixon, P. Kanengoni, N. Kazmi, P. Lufarenko, Z. Lv, S. Sharma, J. Weyn, and S. Xiang, "Ms-nowcasting: Operational precipitation nowcasting with convolutional lstms at microsoft weather," *arXiv preprint arXiv:2111.09954*, 2021.
- [26] J. Jing, Q. Li, X. Peng, Q. Ma, and S. Tang, "Hprnn: A hierarchical sequence prediction model for long-term weather radar echo extrapolation," in *ICASSP 2020-2020 IEEE International Conference on Acoustics, Speech and Signal Processing (ICASSP)*. IEEE, 2020, pp. 4142–4146.
- [27] S. Chen, T. Shu, H. Zhao, Q. Wan, J. Huang, and C. Li, "Dynamic multiscale fusion generative adversarial network for radar image extrapolation," *IEEE Transactions on Geoscience and Remote Sensing*, vol. 60, pp. 1–11, 2022.
- [28] O. Ronneberger, P. Fischer, and T. Brox, "U-net: Convolutional networks for biomedical image segmentation," in *International Conference on Medical image computing and computer-assisted intervention*. Springer, 2015, pp. 234–241.
- [29] K. He, X. Zhang, S. Ren, and J. Sun, "Deep residual learning for image recognition," in *Proceedings of the IEEE conference on computer vision and pattern recognition*, 2016, pp. 770–778.
- [30] S. Woo, J. Park, J.-Y. Lee, and I. S. Kweon, "Cbam: Convolutional block attention module," in *Proceedings of the European conference on computer vision (ECCV)*, 2018, pp. 3–19.
- [31] D. Li, Y. Liu, and C. Chen, "Msdm v1. 0: A machine learning model for precipitation nowcasting over eastern china using multisource data," *Geoscientific Model Development*, vol. 14, no. 6, pp. 4019–4034, 2021.
- [32] A. Vaswani, N. Shazeer, N. Parmar, J. Uszkoreit, L. Jones, A. N. Gomez, Ł. Kaiser, and I. Polosukhin, "Attention is all you need," *Advances in neural information processing systems*, vol. 30, 2017.
- [33] A. Dosovitskiy, L. Beyer, A. Kolesnikov, D. Weissenborn, X. Zhai, T. Unterthiner, M. Dehghani, M. Minderer, G. Heigold, S. Gelly *et al.*, "An image is worth 16x16 words: Transformers for image recognition at scale," *arXiv preprint arXiv:2010.11929*, 2020.
- [34] H. Touvron, M. Cord, A. Sablayrolles, G. Synnaeve, and H. Jégou, "Going deeper with image transformers," in *Proceedings of the IEEE/CVF International Conference on Computer Vision*, 2021, pp. 32–42.
- [35] H. Fan, B. Xiong, K. Mangalam, Y. Li, Z. Yan, J. Malik, and C. Feichtenhofer, "Multiscale vision transformers," in *Proceedings of the IEEE/CVF International Conference on Computer Vision*, 2021, pp. 6824–6835.
- [36] D. Zhou, B. Kang, X. Jin, L. Yang, X. Lian, Z. Jiang, Q. Hou, and J. Feng, "Deepvit: Towards deeper vision transformer," *arXiv preprint arXiv:2103.11886*, 2021.
- [37] Y. Wang, H. Wu, J. Zhang, Z. Gao, J. Wang, S. Y. Philip, and M. Long, "Predrnn: A recurrent neural network for spatiotemporal predictive learning," *IEEE Transactions on Pattern Analysis and Machine Intelligence*, vol. 45, no. 2, pp. 2208–2225, 2022.
- [38] E. N. Anagnostou and W. F. Krajewski, "Real-time radar rainfall estimation. part i: Algorithm formulation," *Journal of Atmospheric and Oceanic Technology*, vol. 16, no. 2, pp. 189–197, 1999.